Available online at www.sciencedirect.com
SCIENCE DIRECT®
International Journal of Heat and Mass Transfer 47 (2004) 1483–1498
International Journal of HEAT and MASS TRANSFER
www.elsevier.com/locate/ijhmt

The finite element model of non-isothermal semi-solid fluid flow

Jerzy Petera *, Monika Kotynia

Faculty of Process and Environmental Engineering, Technical University of Łódź, Wólczańska 213, 93-005 Łódź, Poland

Abstract

A new general non-isothermal rheological model of metal alloys in the thixoforming processes has been derived. The model uses the two-phase approach to flow description with two momentum conservation equations buckled by common pressure and interface drag force. The thixotropy phenomena occurring in the globular structure of the alloy, is modelled by means of an extra kinetic equation describing agglomeration degree. The non-isothermal processes are governed by the thermal energy conservation equation coupled with a temperature–enthalpy and solid fraction relationship. The time evolution of the solid fraction is described by the mass conservation equation for the solid phase with a source term based on the Sheil equation. The mathematical model has been implemented in an original efficient finite element algorithm, which is tested against very well known benchmark problems as well as used in a real 3-D simulation of a thixoforming process.

1. Introduction

The semi-solid metal (SSM) processing is a new technology for near net-shape production of engineering components, in which metal alloys are processed in the temperature range where the liquid and solid phases coexist [1,2]. The semi-solid slurry with a non-dendritic microstructure exhibits a distinct rheological behaviour, namely, thixotropy and pseudo-plasticity [3]. These rheological properties make the SSM processing the unique and effective process for near net-shape product and property enhancement particularly desired in the automobile industry.

With a considerable increase of interest in metal forming using the thixoforming technology during the last years, there is a strong demand for a universal tool for modelling such processes. There is a need for products made of light metal alloys with a high content of aluminium or magnesium. For instance, the automobile industry produces fuel injection systems, steering elements and wheels free of shortcomings usually encountered in traditionally produced casts. The technique of the thixoforming offers better mechanical properties, particularly endurance proof, then precisely filled complicated geometrical casts and energy saving owing to smaller temperature range of the whole process.

Materials cast in the semi-solid state exhibit specific rheological properties like thixotropy and pseudo-plasticity between solidus and liquidus temperatures. The constitutive behaviour of semi-solid alloys is very complex, depending on solid fraction, morphology of the solid phase and thermomechanical history. Although many models are presented in the literature on thixoforming, there is still a need for an adequate model accounting for all of the specific phenomena that taking place during that process. Many of them referred to the thixotropic behaviour only, where metals were treated as homogeneous materials [4], the others took into account two-phase flow, but neglected the thixotropy [5]. While the thixotropy is considered, the model using the agglomeration/dis-agglomeration mechanisms are known [6] based on the definition of a structural parameter. Some more sophisticated models of Alexandrou et al. [7,8], neglect however, the heat transfer during the process. Alexandrou et al. [9] implemented

* Corresponding author. Tel.: +48-42-631-3707; fax: +48-42-636-5663.
E-mail addresses: jpetera@p.lodz.pl (J. Petera), mkotynia@p.lodz.pl (M. Kotynia).

0017-9310/$ - see front matter © 2003 Elsevier Ltd. All rights reserved.
doi:10.1016/j.ijheatmasstransfer.2003.09.019

Nomenclature

c_P	specific heat
C_{ls}	interfacial resistance coefficient
d_p	particle diameter
$\underline{\underline{D}}$	the deformation rate tensor
$\overline{\text{erf}}(\ldots)$	Gauss error function
f	fraction
g	gravity
h	enthalpy
k	consistency coefficient (rheological parameter)
ks	solidification constant (Stefan formulation)
k_p	partition coefficient
L	latent heat
m	power law index (rheological parameter)
ne	equilibrium power law index (rheological parameter)
$\underline{n}$	normal unit vector
N_I	basic function corresponding to node I, in the finite element method
p	pressure
q	interface friction force
$\underline{\underline{S}}$	extra stress tensor
t	time
T	temperature
$\underline{u}$	velocity vector
W_I	weight function
x, y, z	coordinates

Greek symbols

α	upwinding parameter
η	non-Newtonian viscosity
κ	structural parameter
λ	thermal conductivity
λ_i	Lame coefficient
ρ	density
$\dot{\gamma}$	shear rate

Subscripts

B	bulk flow
c	cold surface
e	equilibrium
EQ	equivalent
in	initial
l	liquid phase
M	metal
ref	reference
s	solid phase
Y	yield

Superscript

n	time step

the heat transfer and phase change together with thixotropic behaviour into the commercial simulation package, but did not take into account the phase segregation. Similar approach has been done by Im et al. [10] where the authors investigated extensively such phenomena like the mould filling quality, residual flow and the influence of the natural convection on the solidification process. Models also appeared, in which the mushy region was assumed either to behave like a semi-solid slurry at low solid fractions or a porous medium at high solid fractions [11–13].

It should be emphasized that the thixoforming technology differs essentially from classical methods of metal forming in the way of preparing the material before the actual process. As mentioned above the thixoforming processes operate between the solidus–liquidus temperatures, and the temperature determines the solid fraction in the formed material. Thus it is essential for the quality of the final product to have the exact temperature setting. The heat transfer taking place in the process for a metal alloy is accompanied by the segregation of the chemical constitution coupled with phase-change kinetics, diffusive draining of liquid from the interface front and the convective mixing.

One of the most important issues while dealing with solidification/melting problems is proper determination of the interface position in time. From the numerical stability point of view, the problem with adequate liberation of latent heat is easier to overcome in case when the phase change takes place over a range of temperatures. The issue is in the case of isothermal phase change due to abrupt change of enthalpy. The specific heat experiences the Dirac delta behaviour and an infinitely narrow distance occurs within which the latent heat is liberated. There are essentially two methods for modelling the solidification process, first by use of front tracking on a moving mesh and the other on the fixed-grid. The first one offers better opportunity for accurate front location but can be applied only to simple problems. Since the method involves a moving boundary condition their application is restricted rather to one-dimensional problems or when the interface is distinctly defined. In the other method the evolution of latent heat is accounted for enthalpy determination and whole calculations are carried out on a fixed space grid. The enthalpy, capacitance, fictitious heat flow and temperature recovery techniques can be distinguished among fixed-grid methods.

The most popular from that group is so-called effective heat capacity method. It depends on the evaluation of the gradient dh/dT on the solidification front and can be applied both to the Stefan problems (metals freezing isothermally) and a finite freezing range (mushy zone) of solidification. In the first case, however, there is a need for introducing a small freezing interval. As the result there is a possibility to miss the corresponding front position in space, at which the phase is changing when using too big time step or too large grid size of the computational mesh. There is another risk with the method of direct evaluation of the effective heat capacity connected with its step-like behaviour in the neighbourhood of a freezing front. Some numerical oscillations can appear in the case of iterative solution methods and some averaging techniques must be employed to deal with such problems. Dalhuijsen and Segal [14] recommended the Del Giudice's method, in which the effective heat capacity equation is referred to the orientated direction of the temperature gradient or particularly the Lemmon's method, in which this direction is defined as a normal to the phase change front. The use of the space derivatives of enthalpy and temperature in the effective heat capacity equation ensures that the phase change is likely to be spotted. Although they used the enthalpy gradient in the formulation of the problem, they used specific heat in the thermal energy equation formulation. The authors also recommended using of the mass lumping in order to avoid the numerical oscillations. Sharma et al. [15] proposed another variant of modified specific heat method for calculating the latent heat liberation during solidification of binary alloys. The authors used either the equilibrium relationship or the Sheil equation for determining the rate of the phase change. Occasionally the latter has been incorrectly named as a non-equilibrium approach, despite the fact that still the process was assumed to proceed along the equilibrium curves on the phase diagram with a differential rate. Yoon et al. [4] also considered in their paper the equivalent specific heat method. Although the model was supposed to be suitable for semi-solid alloys, the material has been modelled as a single phase only, which is a major drawback of the work.

Different variants of the general enthalpy approach for determining the heat transfer during the phase-change process have been invented. Swaminathan and Voller [16] have been elaborated the one of the most known variant. In their method the evolution of the latent heat is accounted for by a temperature–enthalpy relationship, which in principle is suitable for alloys and mixtures [17,18]. Since the discontinuity of the enthalpy function is one of the main problems in this method, the inverse function of enthalpy often is used in order to eliminate the step change of enthalpy in case of isothermal solidification [16,19]. In order to avoid the oscillation of the numerical solution and to imitate more precisely the physical reality of the process, Kim and Anghaie [20] proposed an effective conduction length model introduced to the conventional enthalpy method. They assumed, that the heat flux across the boundary of the phase-change cell could be calculated on the basis of the distance between the real interface and the nodal point of neighbouring cell instead of the distance between neighbouring cells. The authors applied their method to one-dimensional Stefan problems and recommended the use of it rather to such cases only.

Swaminathan and Voller [16] proposed well-known step-change enthalpy–temperature relationship in case of pure metals, but their relationship for alloy systems had so many constants, that its universal use is questionable. Particularly time-consuming iterations are necessary for adjustment of non-linear enthalpy–temperature relationship. Basu and Sekhar [21] proposed the model for solidification when both aligned and equiaxed dendrites are forming. They assumed a linear liquid fraction–temperature relationship in the mushy region, expressed in terms of the linearized Sheil equation, which however, is not valid for alloys of lower solute contents.

Various numerical methods have been applied in solving solidification problems like volume of fluid [10], finite difference [22,23], and the finite element [4,16,24].

In the present study an own model of solidification is proposed and examined in a broader context of the thixoforming processes in conjunction with the finite element method. It involves not only thermal issues, but also complex rheological properties of alloys in the semi-solid state. A new variant of the general enthalpy method has been implemented into a general finite element algorithm, in which enthalpy, temperature and the solid fraction are solved simultaneously, thus evading from time consuming iterations typical for adjustments of the mentioned enthalpy–temperature relationships. The thermal energy conservation equation using explicitly the enthalpy as independent variable, is coupled with a mass conservation equation for the solid phase. The latter involves a source/sink term accounting for the rate of the phase change based on the Sheil relationship. The thermal changes are reflected in the rheological equation of state, which influences the flow of each phase. Verification of the model is made on the basis of solutions and experimental results available in the literature. These are analytical solution of the Stefan problem solidification [25,26] and the solidification of the pure metal data published by Gau and Viskanta [27]. A more sophisticated geometry—a real engineering die—was also analysed in terms of assessing the operating conditions for the thixoforming process with such a die.

2. Mathematical model

2.1. Continuity and momentum conservation equations

The mass conservation equation for the bulk flow of an incompressible fluid (particularly two-phase system) is:

$$\underline{\nabla} \cdot \underline{u} = 0 \tag{1}$$

The velocity $\underline{u}$ is defined as the weighted sum of the velocities of individual phases factored by the corresponding fractions of solid f_s and liquid f_l

$$\underline{u} = f_s \underline{u}_s + f_l \underline{u}_l \tag{2}$$

$$f_s + f_l = 1 \tag{3}$$

Particularly a useful relationship can be derived from Eqs. (2) and (3) (to be used later in this text)

$$\underline{u} - \underline{u}_l = f_s(\underline{u}_s - \underline{u}_l) \tag{4}$$

The bulk flow is governed by the general momentum conservation equation in the classical form

$$\rho \frac{D\underline{u}}{Dt} = -\underline{\nabla} p + \underline{\nabla} \cdot \underline{\underline{S}} + \rho \underline{g} \tag{5}$$

$\rho = f_s \rho_s + (1 - f_s)\rho_l$ is the density of the alloy, p the isotropic pressure and $\underline{\underline{S}}$ the extra stress tensor, by which the alloy is modelled as an incompressible non-Newtonian fluid

$$\underline{\underline{S}} = 2\eta_B \underline{\underline{D}} = \eta_B(\underline{\nabla} \underline{u} + \underline{\nabla}^T \underline{u}) \tag{6}$$

with a non-Newtonian shear dependent viscosity as a function of the solid fraction f_s and the state of an internal thixotropic structure variable κ

$$\eta_B = \left(\frac{S_Y(f_s)}{\dot{\gamma}} + k(f_s)\dot{\gamma}^{m(f_s)-1} \right) \cdot \kappa + \eta_0 \tag{7}$$

where

$$\eta_0 = \eta_l(1 + 2.5 f_s + 14.1 f_s^2) \tag{8}$$

is a hypothetical suspension of completely disagglomerated particles when $\kappa = 0$.

The general shear rate is defined as

$$\dot{\gamma} = \sqrt{2II_D} = \sqrt{2Sp(\underline{\underline{D}}^2)} > 0$$

using the second invariant of the deformation rate tensor $\underline{\underline{D}}$. The other parameters in the formula (7): $S_Y(f_s)$, $k(f_s)$ and $m(f_s)$ are the yield stress, consistency and flow index functions of the solid fraction, respectively. The detailed form of these functions was given elsewhere [28].

Then, for the liquid phase, the momentum conservation equation has the following form:

$$\rho_l f_l \frac{D\underline{u}_l}{Dt} = -f_l \underline{\nabla} p + \underline{\nabla} \cdot (f_l \underline{\underline{S}}_l) + \underline{\nabla}(f_l \lambda_l \nabla \cdot \underline{u}_l) + \rho_l f_l \underline{g} + \underline{q} \tag{9}$$

where

$$\underline{\underline{S}}_l = 2\eta_l \underline{\underline{D}}_l = \eta_l(\underline{\nabla} \underline{u}_l + \underline{\nabla}^T \underline{u}_l) \tag{10}$$

ρ_l is the liquid density, p the isotropic pressure and $\underline{\underline{S}}_l$ the extra stress tensors for the liquid phase flow, η_l is constant that is usually in the range of 0.02–0.025 Pa s, which means a Newtonian fluid. Since there is a difference in the phase mobility, and particularly possibility for the phase segregation, the liquid phase is modelled as effectively compressible with the divergence operator for liquid velocity not necessarily equal to zero.

$$\underline{\nabla} \cdot \underline{u}_l \neq 0$$

This justifies the occurrence of the third term on the RHS of Eq. (9) describing this effective compressibility, with the Lame' coefficient λ_i expressed as a function of the Poisson ratio v.

$$\lambda_i = \eta_i \frac{2v}{1 - 2v}, \quad v = 0,5 f_i^2, \quad i = s,l$$

Interface friction force is proportional to the "slip" velocity difference (see also Eq. (4)):

$$\underline{q} = C_{ls}(\underline{u}_s - \underline{u}_l) = \frac{C_{ls}}{f_s}(\underline{u} - \underline{u}_l) \tag{11}$$

In the case of high solid fraction i.e. in the range of about 0.5 or higher, which may occur locally due to the phase segregation, the resistance C_{ls} is large and large adverse pressure gradient must be set up to balance the resistance. In this case Eq. (9) reduces effectively to the Darcy law:

$$C_{ls}(\underline{u}_s - \underline{u}_l) = f_l \underline{\nabla} p \tag{12}$$

C_{ls} is in this regime closely related to the permeability coefficient of the solid phase, which can be described by applying the Carman-Kozeny capillary model. In this model the pores of the solid medium are compared to a system of identical parallel capillaries. The appropriate relationship can be found in the literature [29]

$$C_{ls} = \frac{90\eta_l f_s^2}{f_l^2 d_p^2} \tag{13}$$

and is assumed to be fulfilled for $f_s \geqslant f_{cr}$. This critical value f_{cr} should be taken from a range 0.4–0.5. On the other hand, the interphase drag in the opposite regime of low solid fraction is assumed to be described by an appropriate form resulting from the Stokes law. It was derived in the following form

$$C_{ls} = \frac{18\eta_l f_s}{d_p^2} \tag{14}$$

and is assumed to be fulfilled for $f_s < f_{cr}$.

2.2. Thixotropy kinetical equation

The technical thixoforming is a highly time-dependent process and steady states are never reached. Hence a thixotropic model is important for the simulation of the material flow. Here a thixotropic model is derived on the basis of Moore classical approach [30] with a structural parameter κ, characterizing the degree of agglomeration, which generally depends on the shear rate history. The general equation of state, as given explicitely before by Eq. (7), has a general form

$$\eta = \eta(\dot{\gamma}, \kappa, f_s) \tag{15}$$

The kinetics of the structural parameter (thixotropy kinetical equation) is postulated by the following differential equation:

$$\frac{D\kappa}{Dt} = c(\dot{\gamma}_s) \cdot (\kappa_e - \kappa) \tag{16}$$

As evident from the above equation, any evolution of the structural changes tends to reach an equilibrium described by so-called equilibrium structural

$$\kappa_e = \frac{S_0 + k \cdot \dot{\gamma}_s^{ne}}{S_0 + k^* \cdot \dot{\gamma}_s^{m}} \tag{17}$$

which, however, as a function of the shear rate may change in any flow process.

2.3. Temperature–enthalpy relationships

The thermal energy conservation equation is used here in the following form

$$\frac{Dh}{Dt} = \underline{\nabla} \cdot (\lambda \nabla T) + \eta_B \dot{\gamma}^2 \tag{18}$$

It is assumed that there exists a unique relationship between enthalpy and temperature

$$h(T) = f_s \int_{T_{ref}}^{T} c_s \rho_s \mathrm{d}T + (1 - f_s) \int_{T_{ref}}^{T} c_l \rho_l \mathrm{d}T + (1 - f_s)\rho L \tag{19}$$

$$\rho = f_s \rho_s + (1 - f_s)\rho_l$$

For constant specific heats Eq. (19) can be split into following temperature–enthalpy formulae

$$h = c_s \rho_s (T - T_{ref}) \quad \text{for } T < T_s \tag{19a}$$

$$h = h_s + c_P \rho (T - T_s) + \rho(1 - f_s)L \quad \text{for } h_s < h < h_l \tag{19b}$$

where $h_s = c_s \rho_s (T_s - T_{ref})$ and $h_l = h_s + c_l \rho_l (T_l - T_s) + \rho_l L$

$$h = h_s + c_l \rho_l (T_l - T_s) + \rho_l L + c_l \rho_l (T - T_l) = h_l + c_l \rho_l (T - T_l) \quad \text{for } T > T_l \tag{19c}$$

The above relationships (19a–c) can be thus presented in a concise linear form

$$A_1 T + A_2 h + A_3 f_s = b \tag{20}$$

where

$$A_1 = \begin{cases} c_s \rho_s & \text{for } h < h_s \\ c_P \rho & \text{for } h_s < h < h_l \\ c_l \rho_l & \text{for } h_l < h \end{cases} \tag{21}$$

for melts $A_2 = -1$ and for pure metals

$$A_2 = \begin{cases} -1 & \text{for } h < h_s \\ 0 & \text{for } h_s < h < h_l \\ -1 & \text{for } h_l < h \end{cases} \tag{22}$$

$$b = \begin{cases} c_s \rho_s T_{ref} & \text{for } h < h_s \\ c_P \rho T_s - h_s - \rho(1 - f_s)L & \text{for } h_s < h < h_l \\ c_l \rho_l T_l - h_l & \text{for } h_l < h \end{cases}$$

The solid fraction is determined entirely by enthalpy for pure metals

$$f_s = 1 - \frac{h - h_s}{L} \tag{23}$$

but can be an independent variable for melts in the "mushy state". It is assumed that the kinetic equation for the solid fraction evolution is governed by the mass conservation equation for the solid phase

$$\frac{\partial f_s}{\partial t} + \nabla \cdot (f_s \underline{u}_s) = \frac{\mathrm{d}\tilde{f}_s}{\mathrm{d}T} \frac{DT}{Dt} \tag{24}$$

in which the right-hand side describes the rate of phase change. It is assumed that the phase change is governed by the equilibrium regime described by the Sheil equation

$$\tilde{f}_s = 1 - \left(\frac{T_M - T_L}{T_M - T} \right)^{\frac{1}{1 - k_p}} \tag{25}$$

Hence the derivative on the right hand side is obtained

$$\frac{\mathrm{d}\tilde{f}_s}{\mathrm{d}T} = -\frac{1}{(1 - k_p)(T_M - T_L)} \left(\frac{T_M - T_L}{T_M - T} \right)^{\frac{2 - k_p}{1 - k_p}} \tag{26}$$

3. Numerical algorithm

The numerical algorithm implemented here is based on the fixed-grid methods, in which the interface position is generally at an unknown a priori location between nodes. However in many popular algorithms, particularly adopted in very well known commercial software like FIDAP™ or FLUENT™, the latent-heat

evolution is treated in terms of an equivalent specific heat or equivalently phase change source term.

The idea behind such an approach was to substitute relationship (19a–c) for enthalpy into the thermal energy equation (18) giving for constant density and specific heats

$$\rho c_P \frac{DT}{Dt} = \underline{\nabla} \cdot (\lambda \nabla T) + \eta_B \dot{\gamma}^2 + \rho L \frac{Df_s}{Dt} \tag{27}$$

with the phase change source term on the right hand side. If a relationship between the solid fraction and temperature is specified then Eq. (27) is transformed to

$$\rho c_{EQ} \frac{DT}{Dt} = \underline{\nabla} \cdot (\lambda \nabla T) + \eta_B \dot{\gamma}^2 \tag{28}$$

where the equivalent specific heat is

$$c_{EQ} = c_P - L \frac{\mathrm{d}f_s}{\mathrm{d}T} \tag{29}$$

Rather than specifying a specific heat function, which includes a latent heat jump, an alternative approach is to evaluate the effective specific heat directly from the enthalpy h. For example, the following formula has been used [14] to compute the required specific heat at a point by

$$c_P = \left(\frac{\nabla h \cdot \nabla h}{\nabla T \cdot \nabla T} \right)^{\frac{1}{2}}$$

This expression is computed by first determining the enthalpy at the nodes of the element using the provided enthalpy–temperature curve. As this method incorporates the local distribution of the enthalpy within an element it is able to track the solidification front more accurately than calculated from (29). The drawback is that if the time step is large enough, the proper amount of latent heat will not be released resulting in a faster than desired temperature change.

In most known numerical algorithms Eq. (18) is solved iteratively together with enthalpy–temperature relationship, particularly for melts where the relationship has been sometimes rather cumbersome [16]. This also resulted in a considerable CPU time consumption increase, which is particularly critical issue for solving 3-D problems.

In contrast to previous numerical implementations of the temperature–enthalpy relationships, the use of semi-linear form of Eqs. (abc) has been made when using the solid fraction as an independent variable for melts in the "mushy state". Such an approach has the theoretical background [31]. For the case of pure metals the solid fraction is entirely determined by enthalpy as stated above in Eq. (23) while for melts an evolution equation is derived on the basis of the mass conservation with a source term resulting from the Sheil relationship as in Eq. (25). Thus the system to be solved simultaneously in the time stepping process of the numerical algorithm designed here is as follows:

$$\mathbf{A}^{n+1} \cdot \mathbf{X}^{n+1} = \mathbf{A}^n \cdot \mathbf{X}^n + \mathbf{B} \tag{30}$$

where

$$\mathbf{X}^{n+1} = \begin{bmatrix} \mathbf{T}^{n+1} \\ \mathbf{h}^{n+1} \\ \mathbf{f}_s^{n+1} \end{bmatrix} \quad \mathbf{X}^n = \begin{bmatrix} \mathbf{T}^n \\ \mathbf{h}^n \\ \mathbf{f}_s^n \end{bmatrix} \tag{31}$$

with the coefficient matrices and free term vector as follows:

$$\mathbf{A}^{n+1} = \begin{bmatrix} \Delta t\mathbf{K} & \mathbf{M} + \Delta t\mathbf{C} & \mathbf{0} \\ A_1\mathbf{M} & A_2\mathbf{M} & A_3\mathbf{M} \\ -\frac{\mathrm{d}\tilde{f}_s}{\mathrm{d}T}\mathbf{M} & \mathbf{0} & (1 + \Delta t\chi)\mathbf{M} + \Delta t\mathbf{C} \end{bmatrix} \tag{32}$$

$$\mathbf{A}^n = \begin{bmatrix} \mathbf{0} & \mathbf{M} & \mathbf{0} \\ \mathbf{0} & \mathbf{0} & \mathbf{0} \\ -\frac{\mathrm{d}\tilde{f}_s}{\mathrm{d}T}\mathbf{M} & \mathbf{0} & \mathbf{M} \end{bmatrix} \quad \mathbf{B} = \begin{bmatrix} \mathbf{D} + \mathbf{G} \\ \mathbf{b} \\ \mathbf{0} \end{bmatrix} \tag{33}$$

The detailed formulae resulting from the finite element discretization for the above matrices are given below, where $N_I, N_J, I, J = 1, \ldots, \mathrm{NP}$ are the interpolation basis (shape) functions associated with nodal points of a mesh, NP equal to the number of all nodal points, while W_I, $I = 1, \ldots, \mathrm{NP}$ are the weight functions resulting from the Petrov–Galerkin approach. The latter has been used here to improve the numerical stability, which presents a problem in convection dominated situations.

$$M_{IJ} = \int_\Omega N_I N_J \,\mathrm{d}\Omega, \quad K_{IJ} = \int_\Omega \lambda \underline{\nabla} N_I \cdot \underline{\nabla} N_J \,\mathrm{d}\Omega,$$
$$C_{IJ} = \int_\Omega W_I \underline{v} \cdot \underline{\nabla} N_J \,\mathrm{d}\Omega \tag{34}$$

$$W_I = N_I + \frac{\alpha d}{2|\underline{u}|} \underline{v} \cdot \underline{\nabla} N_I, \quad \alpha = \coth(Pg/2) - 2/Pg,$$
$$Pg = \frac{|\underline{u}|d}{a} = |\underline{u}| d \frac{c_p \rho}{\lambda} \tag{35}$$

$$D_I = \int_\Omega N_I \mu \dot{\gamma}^2 \,\mathrm{d}\Omega, \quad G_I = \int_\Gamma N_I \lambda \underline{\nabla} T \cdot \underline{n} \,\mathrm{d}\Gamma \tag{36}$$

As mentioned above, since in the case of pure metals the solid fraction is entirely determined by enthalpy, there is no need for solving independent solid fraction, and the problem described by Eq. (31) can be reduced considerably. In such case the variables to be actually solved are only temperature and enthalpy, thus

$$\mathbf{X}^{n+1} = \begin{bmatrix} \mathbf{T}^{n+1} \\ \mathbf{h}^{n+1} \end{bmatrix} \quad \mathbf{X}^n = \begin{bmatrix} \mathbf{T}^n \\ \mathbf{h}^n \end{bmatrix}$$

with the coefficient matrices and free term vector as follows:

$$\mathbf{A}^{n+1} = \begin{bmatrix} \Delta t\mathbf{K} & \mathbf{M} + \Delta t\mathbf{C} \\ A_1\mathbf{M} & A_2\mathbf{M} \end{bmatrix} \quad \mathbf{A}^n = \begin{bmatrix} \mathbf{0} & \mathbf{M} \\ \mathbf{0} & \mathbf{0} \end{bmatrix}$$

$$\mathbf{B} = \begin{bmatrix} \mathbf{D} + \mathbf{G} \\ \mathbf{b} \end{bmatrix}$$

The latter case has been found a considerable interest in literature recently. Much less attention has been taken to the melts, which is particularly interesting in context of the thixoforming. The approach presented here making use of solid fraction as an independent variable in the "mushy state" is free of rather cumbersome attempts to define temperature–enthalpy relationship in form of a complicated formulae to fit experimental data. In our case the relationship appears naturally after solving simultaneously the system (30)–(33). The lumping techniques for temperature–enthalpy–solid fraction relationship (19a–c) have been used consistently which resulted in an improved stability algorithm and allowed for reducing the CPU time.

4. Numerical tests

The following numerical tests have been performed for verification of the model and for investigating the rate of convergence of the algorithm.

4.1. Test 1. The Stefan problem—steel solidification

In this test a verification of the model was made by comparison the simulation results with the Stefan–Neumann analytical solution of the one-dimensional solidification problem by conduction. The solidification process takes place in constant temperature and metal properties of both phases are constant and independent of the temperature. Exact specification can be found in literature [25,26]. The functions describing the temperature distribution in solid and liquid part of the mould for the Stefan problem are as follows:

$$T_{sx} = T_c + (T_m - T_c)\frac{\operatorname{erf}\left(\frac{x_s}{2\sqrt{a_s \cdot t}}\right)}{\operatorname{erf}\left(\frac{ks}{2\sqrt{a_s}}\right)} \tag{37}$$

$$T_{lx} = T_{in} - (T_{in} - T_m)\frac{\operatorname{erf}c\left(\frac{x_l}{2\sqrt{a_l \cdot t}}\right)}{\operatorname{erf}c\left(\frac{ks}{2\sqrt{a_l}}\right)} \tag{38}$$

where T_{sx}, T_{lx}—temperature of the solid and liquid cast part, respectively, T_c—temperature of the cast surface (constant along the process), T_{in}—initial temperature of the liquid metal, T_m—melting temperature, x—coordinate in the direction of solidification front moving, t—time, ks—solidification constant, $\operatorname{erf}(\ldots)$–the Gauss error function, a–coefficient of temperature compensation for solid and liquid cast layer, respectively:

$$a_s = \frac{\lambda_s}{c_s \cdot \rho_s}, \quad a_l = \frac{\lambda_l}{c_l \cdot \rho_l}$$

with λ–thermal conductivity. In order to solve Eqs. (37) and (38) the solidification constant ks should be first calculated on the basis of Eq. (39).

$$\frac{b_s(T_m - T_c)}{\operatorname{erf}\left(\frac{ks}{2\sqrt{a_s}}\right)} \exp\left(-\frac{ks^2}{4a_s}\right) - \frac{b_l(T_{in} - T_m)}{\operatorname{erf}c\left(\frac{ks}{2\sqrt{a_l}}\right)} \exp\left(-\frac{ks^2}{4a_l}\right) = \frac{\sqrt{\pi}}{2}\rho_s \cdot L_s \cdot ks \tag{39}$$

where b is the coefficient of heat accumulation for solid and liquid cast part, respectively:

$$b_s = \sqrt{\lambda_s c_s \rho_s}, \quad b_l = \sqrt{\lambda_l c_l \rho_l}.$$

Having calculated solidification constant from Eq. (39), the temperature of solid and liquid part can be obtained either from Eqs. (37) or (38).

Although the problem itself is in fact unidirectional but, for the simulation purpose, an equivalent three-dimensional problem has been designed thus enabling a consistent use of the same 3-D code as in more complex real industrial problems. Thus a steel solidification in a cavity of dimensions $40 \times 1 \times 1$ cm was analysed as depicted in Fig. 1 together with boundary conditions where T is temperature, and h—enthalpy. The mesh, also presented in Fig. 1, had at different variants total number of nodes 4025, 2025 and 1025 and the total number of elements of 15,360, 7680 and 3840 respectively. This corresponded to the longest edge of the cavity divisions of 160, 80 and 40 respectively.

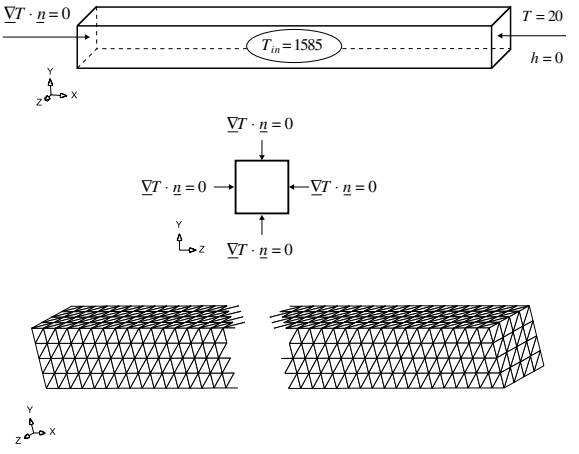

Fig. 1. Initial and boundary conditions for the Stefan problem (the steel solidification) and the mesh used for the numerical modelling.

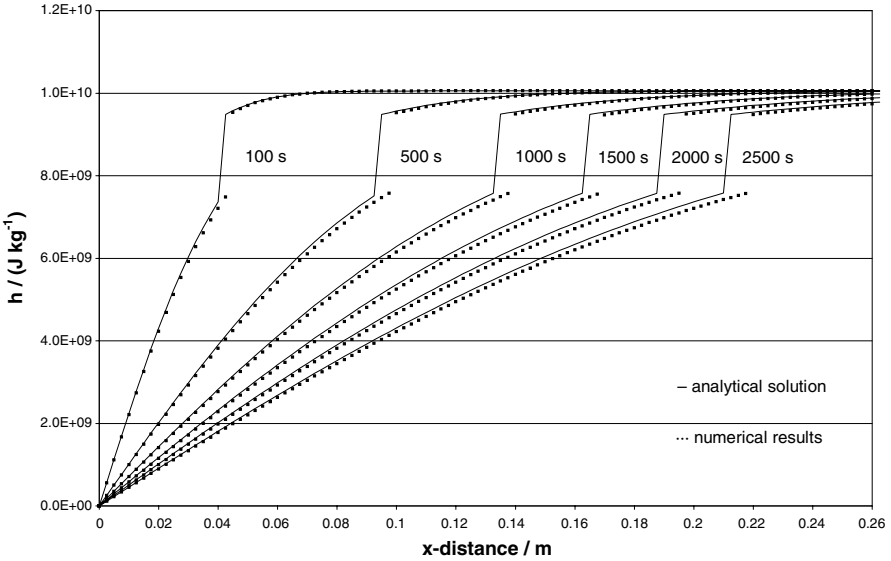

Fig. 2. Comparison of analytically obtained Stefan problem results with numerical simulation by using the traditional specific heat method.

The two methods mentioned above of solving the solidification problems were used: the well-known equivalent specific heat method and the present original variant of the enthalpy method. The analytical solution was compared with the simulation results for both methods, and the result of comparison is shown in Figs. 2 and 3 respectively. The advantage of the new method in terms o accuracy at approximate the same time consumption is obvious. Owing to better numerical stability, the time step for the new method could be increased without a risk of missing the phase-change front. The total CPU time was 4414 s for time step 0.1, 1160 s for time step 0.2 and 599 s with time step 2.0 respectively when using an Intel Pentium 4, 1.8 GHz processor.

The algorithm convergence was checked by using the three mentioned meshes with element dimension coefficient reduced by a factor of 2. The Sobolev norm $\|e\|_0$ of the numerical error e was calculated for any time instant and for different finite element discretization of the computational domain on the basis of the following formula:

$$\|e\|_0 = \sqrt{\frac{1}{b-a}\int_a^b [h_{\text{theor}}(x) - h_{\text{num}}(x)]^2 \mathrm{d}x} \tag{40}$$

where $h_{\text{theor}}(x)$ and $h_{\text{num}}(x)$ are values of the theoretic and numerical solution at a point x, respectively, a, b—beginning and ending of the computational domain along the x-axis.

Fig. 4 presents the error Sobolev norm error as the function of the three characterizing mesh dimensions in the logarithmic plot, calculated at different time instants during simulation run. Simultaneously with mesh division increase, the time step was reduced by the same factor due to the requirement of the error estimation and stability analysis for Lagrange–Galerkin methods. It can be noticed that the error decreases with the mesh refinement, although the most distinctly for the roughest grid (with 40 divisions). The further mesh refinement does not bring significant correction in respect to the numerical error. The conclusion is that the present model has another advantage of reduced sensitivity to mesh refinement and even a relatively crude mesh can be used without loss of accuracy, resulting in reduced CPU time consumption.

4.2. Test 2. The solidification problem of the alloy in the temperature range

The same geometry and meshes as in the *Test 1* were used to simulate the material solidification in a range of temperature. Solidification conditions and thermophysical properties of the Al–4.5%Cu alloy were imposed according to data taken from the literature [16]. The temperature range of freezing was between 548 and 646 °C. The enthalpy–temperature relationship for alloys melting in a range of temperatures is not trivial as mentioned before. Some types of such a relationship for different materials are shown in Fig. 5. Particularly, the curve c is characteristic for metals and alloys freezing in the range of temperature. Fig. 6 presents the Al–Cu example obtained entirely on the basis of numerical results and the mathematical model proves the ability of

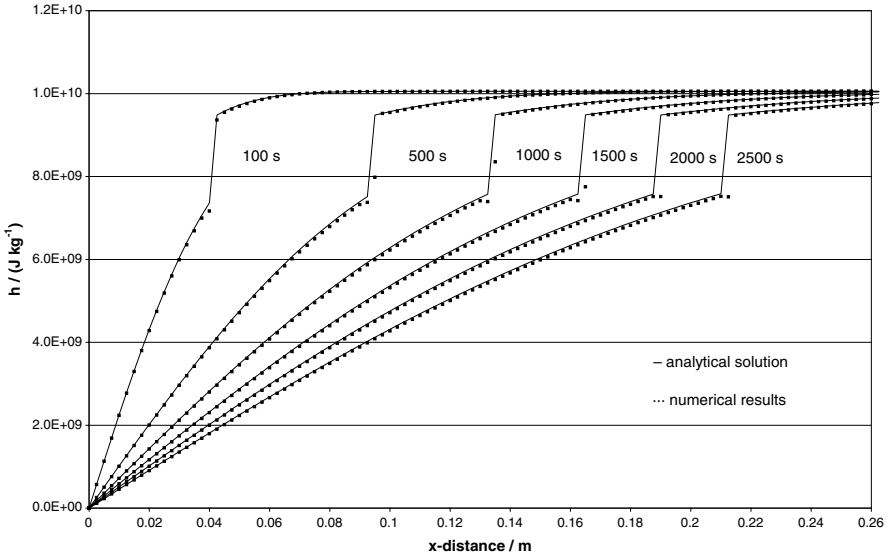

Fig. 3. Comparison of analytically obtained Stefan problem results with numerical simulation by using the present enthalpy method.

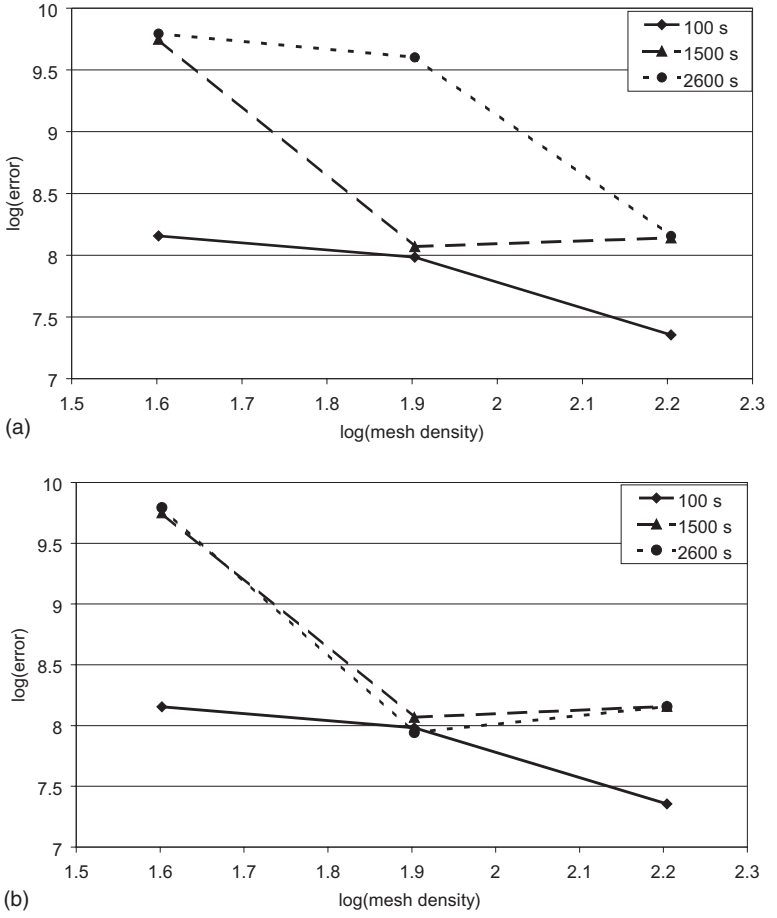

Fig. 4. The error based on the Sobolev norm presented as a function of the characteristic mesh dimension in the logarithmic plot at different times. (a) Time step = 0.1 s and (b) time step = 1 s.

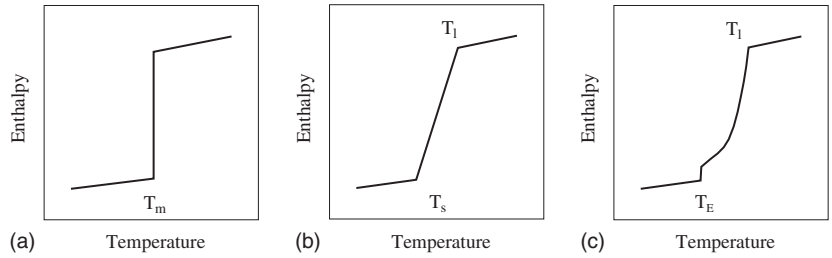

Fig. 5. Different types of the enthalpy–temperature relationship: (a) pure metal, (b) steel, (c) aluminium alloy Al–4.5%Cu [16].

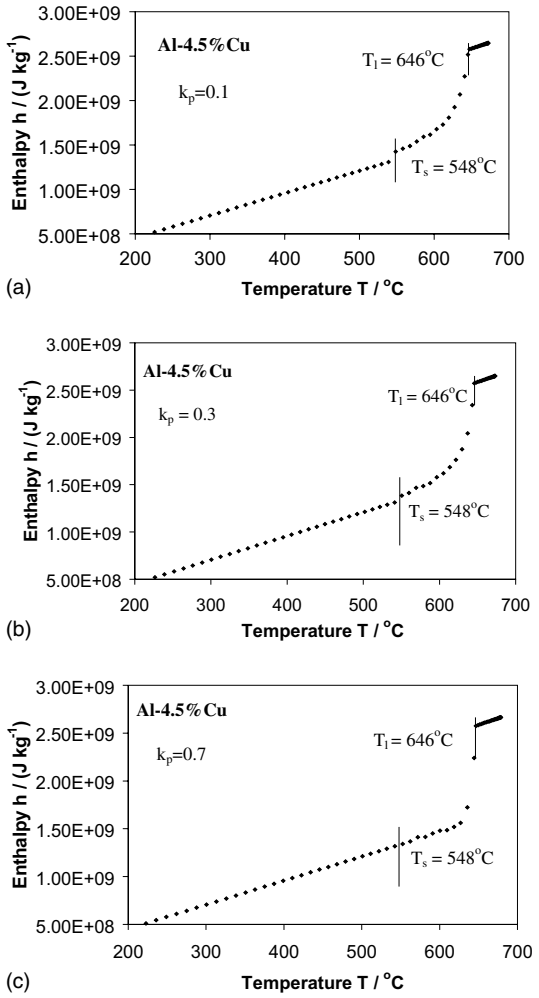

Fig. 6. Enthalpy–temperature relationship for aluminium alloy Al–4.5%Cu obtained from the model.

reflecting the characteristic feature of the enthalpy curve without any reference to empirical data as in fact practiced previously [16].

4.3. Test 3. The melting problem of the solid gallium

The next numerical test used a very well known benchmark problem initiated in the work by Gau and Viskanta [27] concerning melting and solidification of gallium and quoted in the literature very often [17,18,26,32,33]. This particular metal was chosen because of its favourable properties, including a low melting temperature. Unfortunately, the conduction coefficient of gallium is anisotropic, what can cause some problems during simulation. Authors noticed, that although they manage to obtain reproducible results of their experiments in case of melting process, their solidification results were not repeatable, thus the results cannot be trusted unconditionally. It is the natural convection driven problem, thus representing a crucial task for simulation. Originally, the computational domain was a rectangle cavity of the main dimensions of 8.89×6.35 cm. As in previous tests the computational domain was extended to the third dimension along the z-axis in the own simulations and presented in Fig. 7 together with initial and boundary conditions. The mesh was analogical to the one shown in Fig. 1, consisting as before of the tetrahedral elements, with the main divisions $30 \times 25 \times 1$. The velocity field and the melting front movement at different three time instants are depicted in Fig. 8. Since the data available in the literature were used for the verification of the model, the obtained results compared with previous works are presented in Fig. 9. The results appeared to be sensitive to the upwinding parameter α, which has been adjusted by a trial-and-error method. A modification of the upwinding techniques together with corrected conductivity property is expected to give even better agreement with the experimental data.

4.4. Test 4. The solidification problem of the aluminium alloy

Im et al. in their paper [10] specified the problem, although the authors did not present the experimental results. The only verification can be made on the basis of

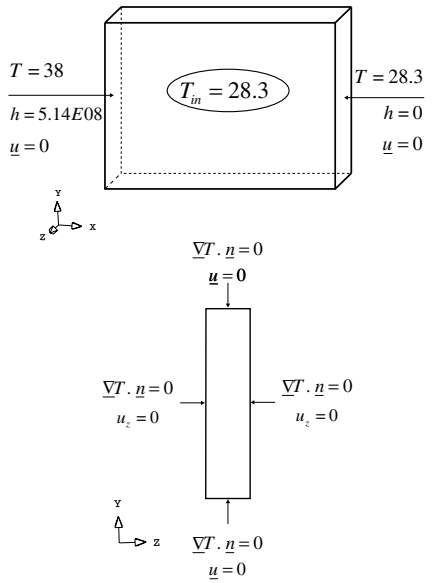

Fig. 7. Problem specification for the gal melting benchmark problem with the initial and boundary conditions.

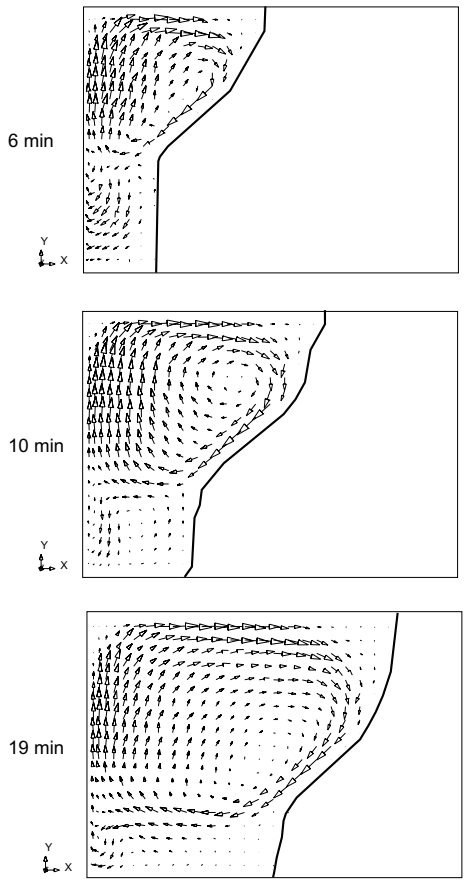

Fig. 8. The evolution of the velocity field and the melting front position at three selected time instants during the gal melting process.

the numerical results qualitative comparison. The content of aluminium alloy is not precisely defined in their paper. The test however has been used here for simulation of the phase change phenomena occurring in a range of temperatures. As in the case of pure gallium the mechanism was driven by the natural convection. The square cavity of the main dimensions of 0.05×0.05 m extended again to third dimension was used as the computational domain and is shown in Fig. 10 together with initial and boundary conditions. The solidification was realized by fixing the temperature of 500 °C to the left wall of the cavity, while the other walls were insulated, except the right one, which was maintained at 700 °C throughout the whole experiment. The mesh was regular consisting of the 10500 elements with total number of nodes equal to 2808. The time step was set to 0.2. The velocity field and the temperature profile at a selected instant 30 seconds (as used in the literature) are presented in the Fig. 11. In the second plot the isotherms corresponding to the solidus −550 °C and liquidus −650 °C temperatures can be seen. The flow patterns as well as the temperature field is consistent with the physics and compares very well to the literature data.

4.5. Test 5. A complex simulation test concerning the thixoforming technology of the aluminium alloy

In order to validate the model in terms of assessing the operating conditions for the thixoforming process in a more complex geometry, a real die was analysed. The original element—a bracket of a car engine support

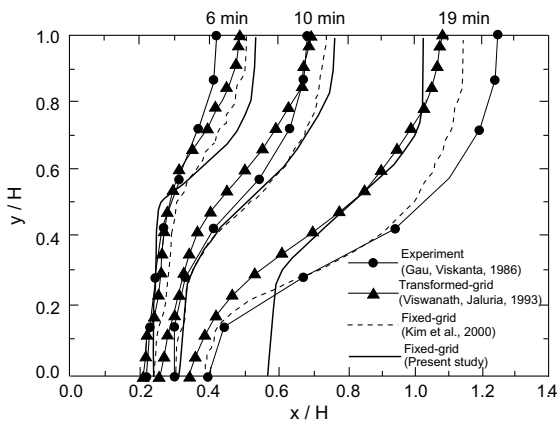

Fig. 9. Comparison of the simulation results obtained from the present numerical algorithm for the gal melting problem with available experiment and previous works.

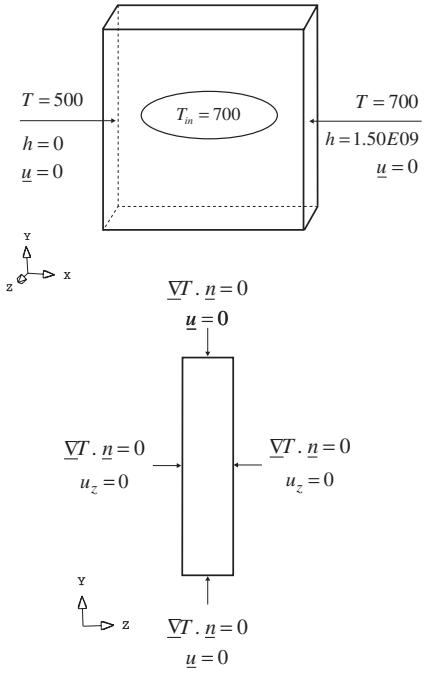

Fig. 10. Problem specification for an aluminium alloy solidification with initial and boundary conditions.

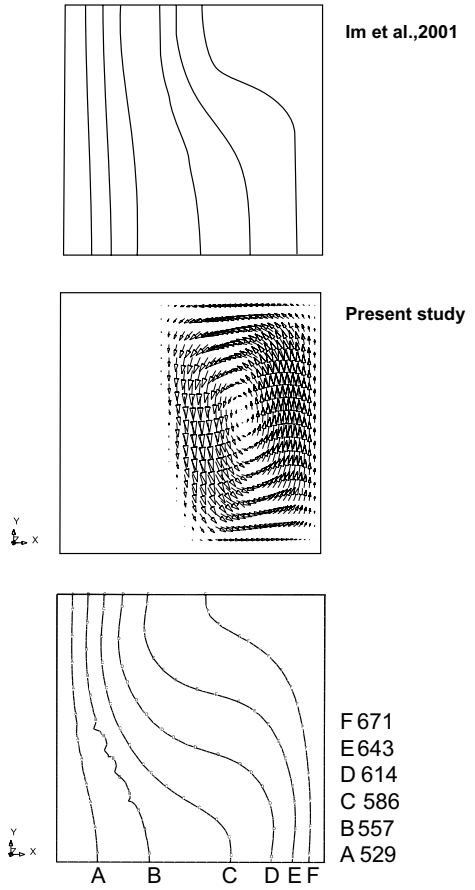

Fig. 11. The velocity field and the temperature profile at a selected instant of simulation for an aluminium alloy solidification problem.

produced by Polish WSK PZL-Rzeszów S.A. factory was chosen for verification. This element was made of aluminium alloy AlSi7Mg (AK7 according to the Polish norm) normally made with the use of a gravity mould. The initial temperature of the alloy used with gravitational process was 700 °C. For the thixoforming simulation the initial temperature was set to 600 °C. The temperature equal 255 °C and velocity $\underline{u} = 0$ were set on all external surfaces, except inlet surface where the velocity of 5 m/s was imposed, as the boundary conditions.

The mesh was prepared using the commercial software ANSYS® and then transformed via a specially written interface to the format acceptable by the own simulation software. Its schematic picture is presented in the Fig. 12 with indicating the inlet and outlet points and the positions of thermocouples. The mesh consisted of tetrahedral elements, with the total number of nodes and elements equal 6637 and 24887, respectively.

Simulations of a hypothetical transient thixoforming process were done using the own simulation software in time stepping algorithm outlined before. All three velocity fields, the bulk one and for both individual phases were simulated, simultaneously with temperature, enthalpy, and solid fraction fields according to the algorithm described above. Total CPU time consumption was 6 h on Intel Xeon 2.4 GHz. The simulation results were exported to the commercial software FEMGV® via another interface program for the purpose of visualization.

Fig. 13 shows the simulated bulk velocity field while Fig. 14–the simulated pressure field. The maximum calculated pressure value was 0.3E8Pa (not readable direcly from the Fig. 14 because of non-uniform scale used for visualization). Thus the required press recommended for use in an adequate operation should have power sufficient to produce at least 300 MPa. For comparison, analogical simulated pressure field for the gravitational moulding counterpart is presented in Fig. 15 reflecting well the hydrostatic pressure. Then, Fig. 16 shows different stages of thixoforming in terms of free surface progress and the correspondent solid fraction field evolution. The contours were obtained in cross-section area as specified in Fig. 12. A good thixoformability is predicted, providing the proper equipment is available. Fig. 17 presents the comparison of temperature at the thermocouples positions measured vs. simu-

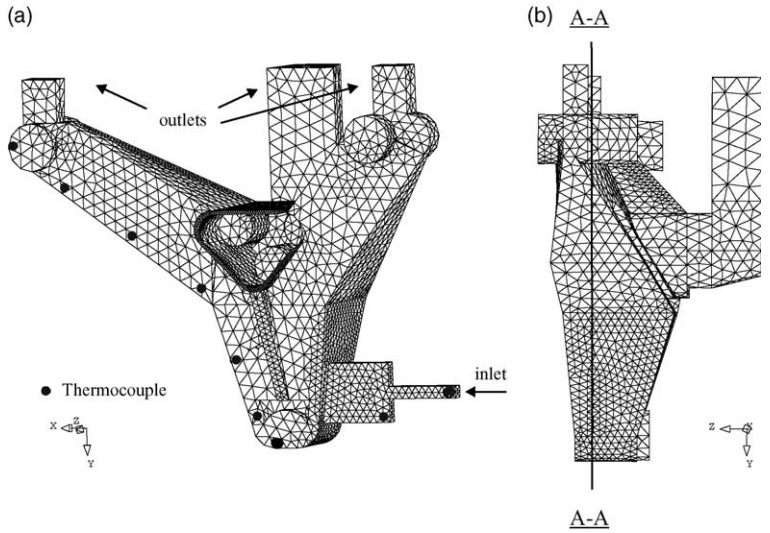

Fig. 12. The computational mesh for the test concerning a car engine support: (a) thermocouples positions, (b) the position corresponding to the cross-sectional area used in Fig. 16.

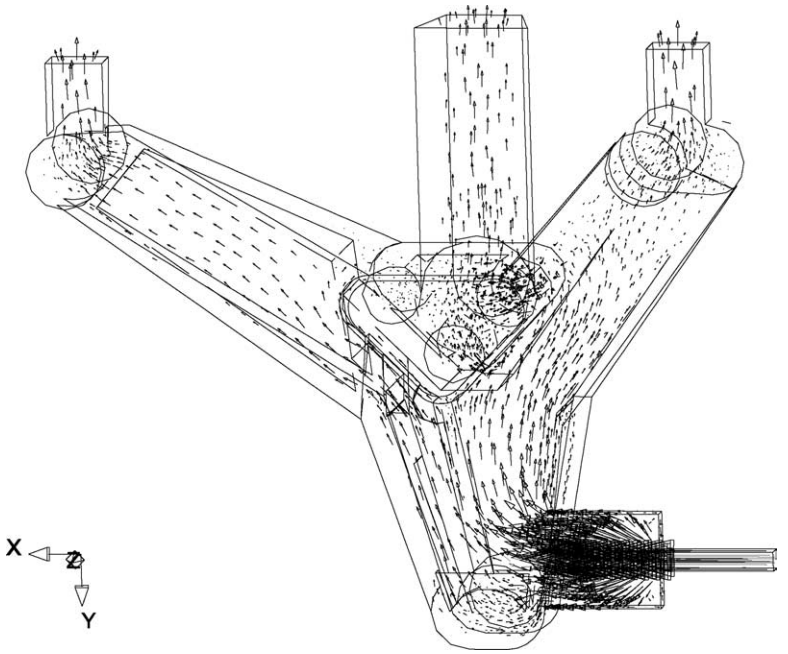

Fig. 13. Simulated bulk velocity field for thixoforming process in the complex geometry.

lated (two first locations were omitted since they were inconsistent with imposed boundary conditions for the purpose of simulation). Although the values were mostly determined by the boundary conditions, nevertheless good agreement can be observed.

5. Conclusions

The mathematical model represents a unified universal approach to thermodynamical description of metal alloys processing including the semi-solid state as

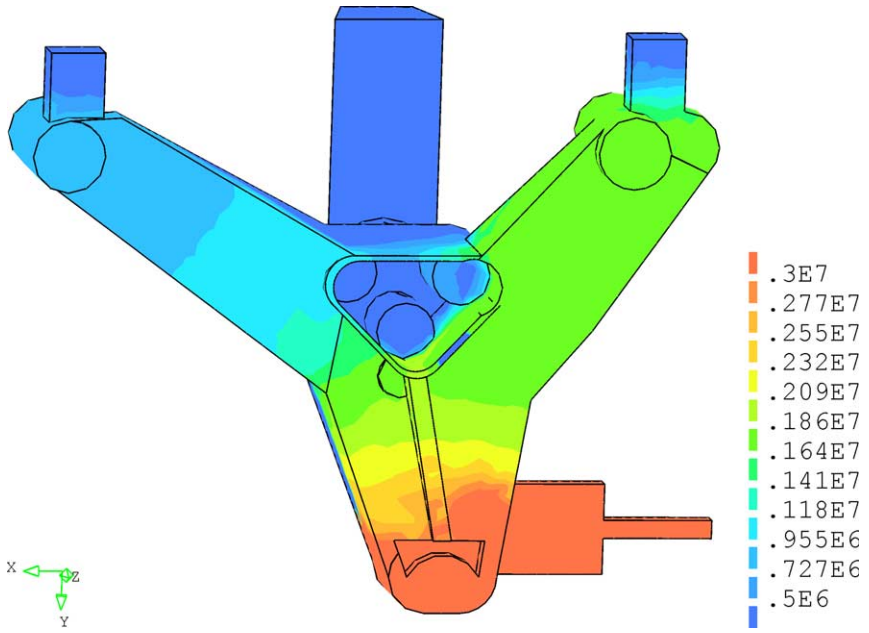

Fig. 14. Simulated pressure field for thixoforming process in the complex geometry.

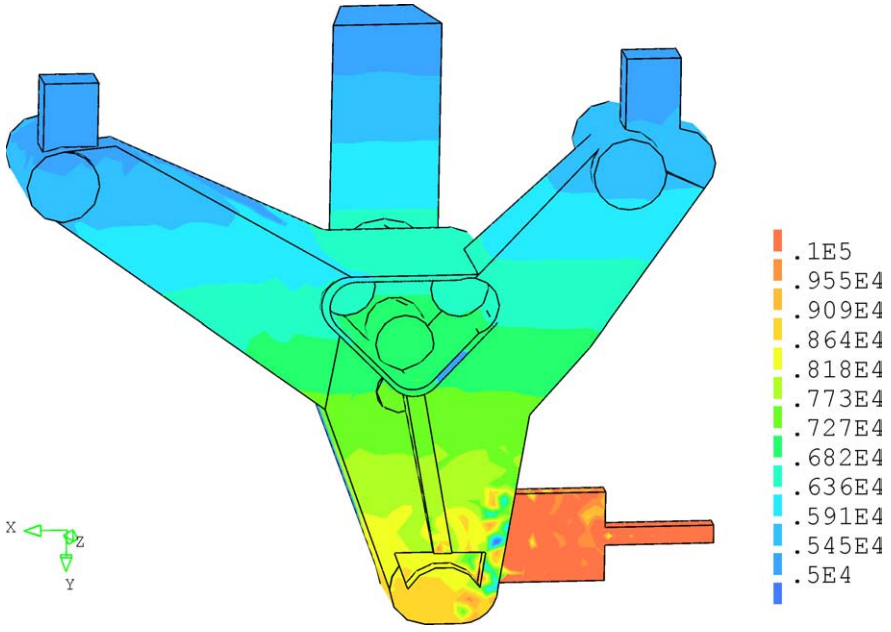

Fig. 15. Simulated pressure field for gravitational process in the complex geometry.

encountered in the thixoforning technology. First of all, two-phase approach to flow description of metal alloys in the semi-solid state is fully adopted, allowing for simulation of the phase segregation being a characteristic feature and a real problem in thixoforming processes. The interface drag force is modelled consistently using ether Carman–Kozeny or Stokes law, depending on the local value of solid fraction allowing for a broad range of solid fraction conditions. Secondly, the time-dependent phenomena like thixotropy resulting from

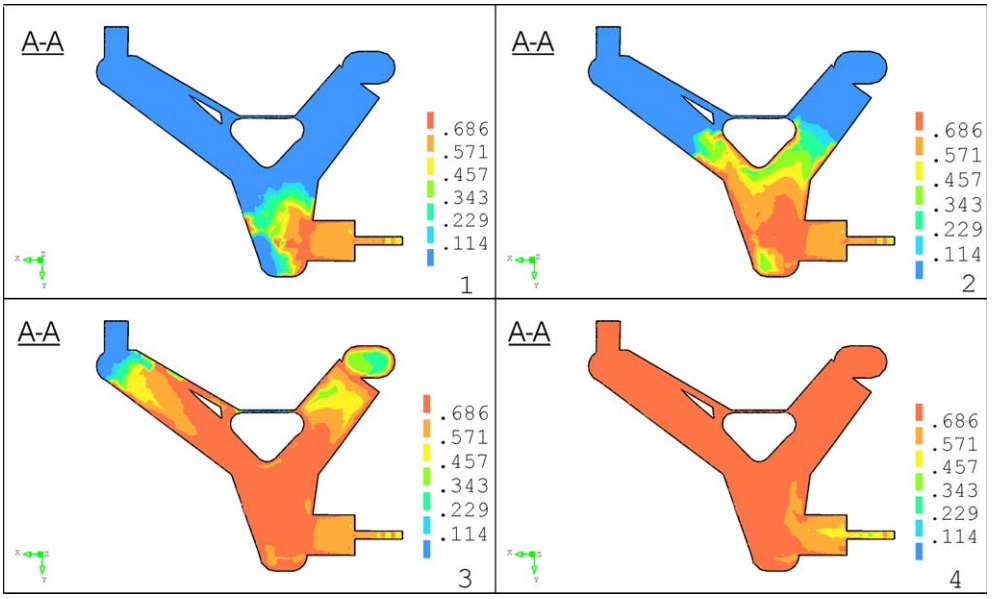

Fig. 16. Different stages of thixoforming in terms of free surface progressing and the correspondent solid fraction fields.

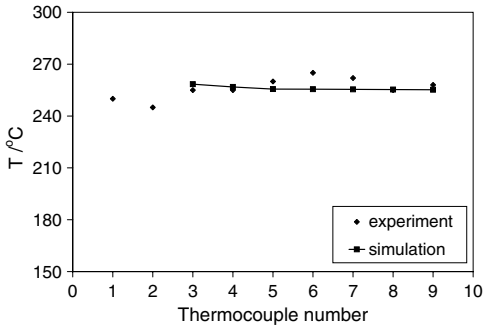

Fig. 17. Comparison of measured vs. simulated temperature at the thermocouples positions.

agglomeration phenomena occurring naturally in globular structure of the alloy are reflected in the model. Then, the non-isothermal phase change is described in terms of temperature–enthalpy–solid fraction relationships simultaneously, resulting in an efficient algorithm for calculation of the corresponding fields evolution in time on the domain. Particularly, this includes the phase-change front tracking in arbitrary 3-D flow conditions on a fixed mesh.

The numerical algorithm is free of time-consuming iterations for mutual adjustment of the temperature–enthalpy relationships, thus is suitable for 3-D simulations using even an ordinary PC. Moreover, owing to better numerical stability, the time step for the new method could be increased without a risk of missing the phase-change front.

Acknowledgements

This research was supported by the Polish State Committee for Scientific Research by means of Grant no. 3 T09C 025 19.

References

[1] M.C. Flemings, Behavior of metal alloys in the semisolid state, Metall. Trans. A 22A (1991) 957–981.
[2] D.H. Kirkwood, Semisolid metal processing, Int. Mater. Rev. 39 (1994) 173–189.
[3] P.A. Joly, R. Mehrabian, The rheology of a partially solid alloy, J. Mater. Sci. 11 (1976) 1393–1418.
[4] J.-H. Yoon, Y.-T. Im, N.-S. Kim, Finite element modeling of the deformation behavior of semi-solid materials, J. Mater. Process. Technol. 113 (2001) 153–159.
[5] A. Zavaliangos, Modeling of the mechanical behavior of semisolid metallic alloys at high volume fractions of solid, Int. J. Mech. Sci. 40 (1998) 1029–1041.
[6] C.L. Martin, S.B. Brown, D. Favier, M. Suery, Shear deformation of high solid fraction (>0.60) semi-solid Sn–Pb under various structures, Mater. Sci. Eng. A A202 (1995) 112–122.
[7] A.N. Alexandrou, G.R. Burgos, V. Entov, Two-phase model for processing materials in semisolid state, Proceedings of the Fifth International Conference on Semi Solid Processing of Alloys and Composites, Colorado School of Mines in Golden, Colorado, 1998.
[8] A.N. Alexandrou, Y. Pan, D. Apelian, G. Georgiou, Semisolid material characterization using computational rheology, Proceedings of the Fourth S2P 2002, International Conference on Semi-Solid Processing of Alloys and Composites, Tsukuba, Japan, 2002.

[9] A.N. Alexandrou, F. Bardinet, W. Loué, Mathematical and computational modeling of die filling in semisolid metal processing, J. Mater. Process. Technol. 96 (1999) 59–72.
[10] I.-T. Im, W.-S. Kim, K.-S. Lee, A unified analysis of filling and solidification in casting with natural convection, Int. J. Heat Mass Transfer 44 (2001) 1507–1515.
[11] O.J. Ilegbusi, M.D. Mat, An internal–variable constitutive model for semisolid slurries at high solid fraction, J. Mater. Eng. Perform. 7 (2) (1998) 199–204.
[12] O.J. Ilegbusi, M.D. Mat, Modeling flowability of mushy zone with a hybrid model utilizing coherency solid fraction, Mater. Sci. Eng. A A247 (1998) 135–141.
[13] M.D. Mat, O.J. Ilegbusi, Application of a hybrid model of mushy zone to macrosegregation in alloy solidification, Int. J. Heat Mass Transfer 45 (2002) 279–289.
[14] A.J. Dalhuijsen, A. Segal, Comparison of finite element techniques for solidification problems, Trans. ASME, J. Eng. Mater. Technol. 23 (1986) 1807–1829.
[15] D.G.R. Sharma, M. Krishnan, C. Ravindran, Determination of the rate of latent heat liberation in binary alloys, Mater. Character. 44 (2000) 309–320.
[16] C.R. Swaminathan, V.R. Voller, A general enthalpy method for modeling solidification processes, Metall. Trans. B 23B (1992) 651–664.
[17] Y. Jaluria, Numerical modeling of materials processing systems, Computat. Mech. 21 (1998) 199–210.
[18] J.A. Dantzig, Modeling solidification processes using FIDAP, Crystal Res. Technol. 34 (4) (1999) 417–424.
[19] B. Minaie, K.A. Stelson, V.R. Voller, Analysis of flow patterns and solidification phenomena in the die casting process, Int. J. Num. Meth. Eng. 113 (1991) 296–302.
[20] S. Kim, S. Anghaie, An effective conduction length model in the enthalpy formulation for the Stefan problem, Int. Commun. Heat Mass Transfer 28 (6) (2001).
[21] B. Basu, J.A. Sekhar, Modeling of multidimensional solidification of an alloy, Metall. Trans. A 20A (1989) 1833–1845.
[22] J.F. McCarthy, N.W. Blake, A front tracking model for the rapid solidification of dendritic alloys, Acta Metall. 44 (5) (1996) 2093–2100.
[23] L.-S. Chao, W.-C. Du, Macro–micro modeling of solidification, Proceedings of the National Science Council, ROC Part (A) 23 (5) (1999) 622–629.
[24] J.C. Choi, J.H. Park, B.M. Kim, Finite element analysis of the combined extrusion of semi-solid material and its experimental verification, J. Mater. Process. Technol. 105 (2000) 49–54.
[25] W. Longa, Krzepnięcie odlewów, Wydawnictwo Śląsk, Katowice, 1985, pp. 176–190.
[26] Q. Duan, F.L. Tan, K.C. Leong, A numerical study of solidification of n-hexadecane based on the enthalpy formulation, J. Mater. Process. Technol. 120 (2002) 249–258.
[27] C. Gau, R. Viskanta, Melting and solidification of a pure metal on a vertical wall, J. Eng. Mater. Technol.–Trans. ASME 108 (1986) 174–181.
[28] M. Kotynia, J. Petera, Model matematyczny stopów metali w stanie półpłynnym, Inżynieria Chemiczna i Procesowa 22 (2001) 323–343.
[29] Z. Kembłowski, S. Michałowski, C. Strumiłło, R. Zarzycki, Podstawy teoretyczne iżnynierii chemicznej i procesowej, WNT, Warszawa, 1985, pp. 156–158.
[30] F. Moore, The rheology of ceramic slips and bodies, Trans. British Ceramic. Soc. 58 (1959) 470–494.
[31] G. Astarita, G. Marrucci, Principles of Non-Newtonian Fluid Mechanics, McGraw-Hill, London, 1974.
[32] A.D. Brent, V.R. Voller, K.J. Reid, Enthalpy–porosity technique for modeling convection–diffusion phase change: application to the melting of a pure metal, Num. Heat Transfer 13 (1988) 297–318.
[33] S. Kim, S. Anghaie, G. Chen, A fixed-grid analysis of convection-dominated melting and solidification, in: Proceedings of the Trends in Numerical and Physical Modeling for Industrial Multiphase Flows, Institute d'Etudes Scientifiques de Corgese, France, 2000.